

# Nanoscale

Accepted Manuscript



This is an *Accepted Manuscript*, which has been through the Royal Society of Chemistry peer review process and has been accepted for publication.

*Accepted Manuscripts* are published online shortly after acceptance, before technical editing, formatting and proof reading. Using this free service, authors can make their results available to the community, in citable form, before we publish the edited article. We will replace this *Accepted Manuscript* with the edited and formatted *Advance Article* as soon as it is available.

You can find more information about *Accepted Manuscripts* in the [Information for Authors](#).

Please note that technical editing may introduce minor changes to the text and/or graphics, which may alter content. The journal's standard [Terms & Conditions](#) and the [Ethical guidelines](#) still apply. In no event shall the Royal Society of Chemistry be held responsible for any errors or omissions in this *Accepted Manuscript* or any consequences arising from the use of any information it contains.

## ARTICLE

# Highly monodisperse low-magnetization magnetite nanocubes as simultaneous $T_1$ - $T_2$ MRI contrast agents

Cite this: DOI: 10.1039/x0xx00000x

V. K. Sharma,<sup>a,b</sup> A. Alipour,<sup>a</sup> Z. Soran-Erdem,<sup>a</sup> Z. G. Aykut<sup>a</sup> and H. V. Demir<sup>a,b</sup>

Received 00th February 2015,

Accepted 00th February 2015

DOI: 10.1039/x0xx00000x

www.rsc.org/

We report the first study of highly monodisperse and crystalline iron oxide nanocubes with sub-nm controlled size distribution ( $9.7 \pm 0.5$  nm in size) that achieve simultaneous contrast enhancement in both  $T_1$ - and  $T_2$ -weighted magnetic resonance imaging (MRI). Here, we confirmed the magnetite structure of iron oxide nanocubes by x-ray diffraction (XRD), selected area electron diffraction (SAED) pattern, optical absorption and Fourier transformed infrared (FT-IR) spectra. These magnetite nanocubes exhibit superparamagnetic and paramagnetic behavior simultaneously by virtue of their finely controlled shape and size. The magnetic measurements reveal that the magnetic moment values are favorably much lower because of the small size and cubic shape of the nanoparticles, which results in enhanced spin canting effect. As a proof-of-concept demonstration, we showed their potential as dual contrast agents for both  $T_1$ - and  $T_2$ -weighted MRI via phantom studies, *in vivo* imaging and relaxivity measurements. Therefore, these low-magnetization magnetite nanocubes, while being non-toxic and bio-compatible hold great promise as an excellent dual-mode  $T_1$ - $T_2$  contrast agent for MRI.

## Introduction

Magnetic nanoparticles have been used as contrast agents for magnetic resonance imaging (MRI)<sup>1,2</sup>, drug delivery vehicles<sup>3</sup>, and magnetic separation.<sup>4</sup> Among them, MRI is one of the most powerful medical diagnostic tools because it can provide images in a noninvasive manner together with real-time monitoring capability featuring excellent anatomical details based on the soft tissue contrast and functional information.<sup>5</sup> The sensitivity of MRI can be greatly improved by using contrast agents that enhance the contrast of the region of interest from the background. The MRI contrast agents are generally categorized according to their effects on longitudinal ( $T_1$ ) and transversal ( $T_2$ ) relaxations, and their respective ability is referred to as longitudinal ( $r_1$ ) and transversal ( $r_2$ ) relaxivity. The region where  $T_1$  relaxation takes place appears brighter, whereas  $T_2$  relaxation results in a darker contrast in the MR images.  $T_1$ -based contrast agents are thus also called as positive contrast agents, whereas  $T_2$  counterparts are also known as negative contrast agents.

Superparamagnetic iron oxide (SPIO) nanoparticles (NPs) with strong magnetic moments are the prevailing  $T_2$  contrast agents, especially in the imaging and detection of lesions from normal tissues.<sup>6</sup> The significant drawbacks of these  $T_2$  contrast nanoparticles are, however, magnetic susceptibility artifacts and negative contrast effects, which may limit their clinical applications. On the contrary,  $T_1$  imaging, typically using paramagnetic materials as the contrast agents, provides an excellent resolution between tissues due to its high signal intensity. Gadolinium (Gd) and manganese (Mn) based species are the most commonly used  $T_1$  contrast agents in clinics.<sup>7,8</sup> With unique advantages on their own, combining  $T_1$  and  $T_2$  imaging capabilities into a single type of contrast agent for MRI attracts considerable interest because this can give accurate diagnostic information. As a result, this creates strong motivation for designing new strategies to obtain synergistically enhanced  $T_1$  and  $T_2$  dual

modal contrast agents (DMCAs) for MRI. There are few reports<sup>9-14</sup> on the DMCAs with both  $T_1$  and  $T_2$  capabilities for MRI.  $Mn_xFe_{1-x}O$  nanocrystals have been reported as potential DMCAs by different groups.<sup>9,11</sup> It was found that a specific composition results in simultaneous  $T_1$  and  $T_2$  contrast enhancement effects, which stems from different magnetic moments of the constituent  $Mn^{2+}$  and  $Fe^{2+}$  ions.<sup>15</sup> Gadolinium-labeled magnetite nanoparticles (GMNPs)<sup>12</sup> synthesized via conjugation of gadolinium and magnetite nanoparticles have also been reported as potential DMCAs. Zhou *et al.*<sup>10</sup> demonstrated monodisperse gadolinium iron oxide (GdIO) nanoparticles as DMCAs synthesized using a magnetically decoupled core-shell design.<sup>16</sup> In this design, GdIO nanoparticles were obtained by embedding the paramagnetic  $Gd_2O_3$  species into superparamagnetic  $Fe_3O_4$  nanoparticles. However, although gadolinium (Gd)<sup>17</sup> has been the most popular choice among the paramagnetic metals, it has been recently linked to a medical condition known as nephrogenic systemic fibrosis (NSF).<sup>7</sup> For obvious reasons, this has led to concerns over the safety of Gd-based  $T_1$  contrast agents in MRI applications.

Iron oxide NPs are still considered to be the best materials for MRI applications.<sup>18</sup> They are more biocompatible than Gd and Mn based materials because the iron species are rich in human blood, which are mostly stored as ferritin in the body. Cytotoxicity investigations also confirmed that the iron oxides NPs are well tolerated by the human body.<sup>19-22</sup> However, common iron oxide NPs are not appropriate for the  $T_1$  MRI contrast agents. Although ferric ( $Fe^{3+}$ ) ions having 5 unpaired electrons increase the  $r_1$  value, the high  $r_2$  of iron oxide nanoparticles derived from innate high magnetic moment prevents them from being utilized as  $T_1$  contrast agent. This problem can be resolved by decreasing size of the magnetic nanoparticles. The magnetic moment of magnetic nanoparticles rapidly decreases as their size decreases due to the reduction in the volume magnetic anisotropy and spin disorders on the surface of the nanoparticles. Recently, Kim *et al.*<sup>23</sup> reported 3

nm sized spherical iron oxide nanoparticles as a potential candidate for  $T_1$  contrast agents, with high  $r_1$  relaxivity of  $4.78 \text{ mM}^{-1}\text{s}^{-1}$ . On the other hand, Lee *et al.*<sup>22</sup> reported extremely high  $r_2$  relaxivity ( $761 \text{ mM}^{-1}\text{s}^{-1}$ ) for the ferrimagnetic iron oxide nanocubes of 22 nm size. Very recently, Li *et al.*<sup>24</sup> reported dual modal MRI contrast capabilities from ultrasmall iron oxide nanoparticles. They reported high longitudinal relaxivity  $r_1=8.3 \text{ mM}^{-1}\text{s}^{-1}$  but the transverse relaxivity is comparatively lower  $r_2=35.1 \text{ mM}^{-1}\text{s}^{-1}$ . A careful observation of the result suggests that if we increase the size of the iron oxide NPs,  $r_1$  relaxivity will decrease and  $r_2$  relaxivity will increase. MR relaxivity is strongly related to the size and shape of the nanoparticles. Zhen *et al.*<sup>25</sup> observed that iron oxide nanoparticles with cubic geometry possess high relaxivity values (up to 4 times stronger) in comparison to the spherical counterparts. Therefore, size- and shape-controlled synthesis of uniform nanoparticles is critical for the fine control of MR relaxivity. In the previous works, iron oxide nanoparticles have not been reported as efficient dual modal contrast agent in MRI. The issue is, if we decrease the size too much they compromised the  $T_2$  contrast capabilities of these NPs and vice versa. Recently, Zhou *et al.*<sup>26</sup> regulate the balance of  $T_1$  and  $T_2$  contrast by controlling structure and surface features, including morphology, exposed facets, and surface coating. Also, Iron oxide nanoparticles are commonly known to possess magnetite ( $\text{Fe}_3\text{O}_4$ ) or maghemite ( $\text{Fe}_2\text{O}_3$ ) crystal structure, which are quite difficult to differentiate only on the basis of XRD measurements. But a careful observation of the previous reports, reveals that, they also lacks detailed characterization to differentiate between magnetite ( $\text{Fe}_3\text{O}_4$ ) or maghemite ( $\text{Fe}_2\text{O}_3$ ) crystal structure of the iron oxide NPs.

In this article, we report the synthesis of highly monodisperse and crystalline iron oxide nanocubes for simultaneous contrast enhancement in both  $T_1$ - and  $T_2$ -weighted MRI. We also performed a detailed characterization to confirm the magnetite structure of the iron oxide nanocubes. These nanocubes were successfully demonstrated as DMCA in phantom experiments and *in vivo* MRI. Also, these nanocubes are small in size (9.7 nm) and can be used in most parts of the human body.<sup>7,27</sup> These nanocubes are unique in that, being smaller in size, they offer simultaneous  $T_1$  and  $T_2$  contrast enhancement in MRI while being safer for the body. To the best of our knowledge, this is the first report of dual contrast enhancement in  $T_1$ - and  $T_2$ -weighted MR images using magnetite nanocubes.

## Experimental Section

### Materials

Ammonia (28 wt % in water), poly(5)oxyethylene-4-nonylphenyl-ether (Igepal Co 520), tetraethyl orthosilicate (TEOS, 99%), oleic acid (tech 90%), 1-octadecene (tech90%) and iron (II) chloride hexahydrate (99.99%) were purchased from Sigma-Aldrich. Sodium hydroxide, ethanol, hexane, cyclohexane and other reagents were purchased from Alfa Aesar. All chemicals were used as received without further purification.

### Synthesis of sodium oleate

Sodium oleate was made by adding sodium hydroxide (0.71 g, 17.6 mmol) to oleic acid (5.56 mL, 17.6 mmol) dissolved in ethanol (50 mL). The reaction mixture was stirred overnight at room temperature. Removal of the solvent under vacuum yielded the product as a white soap.

### Synthesis of iron-oleate complex

In a typical procedure, iron chloride ( $\text{FeCl}_2 \cdot 6\text{H}_2\text{O} \sim 0.9 \text{ g}$ , 5 mmol) and sodium oleate (4.56 g, 15 mmol) were mixed in a round bottom flask with distilled water (60 mL), ethanol (25 mL) and hexane (25 mL) to generate Fe-oleate complex. The reaction system was allowed to perform at  $90 \text{ }^\circ\text{C}$  for 4 h before cooling to room temperature. When the reaction was completed, the upper organic layer containing the Fe-oleate complex was washed two times with distilled water in a separatory funnel. After washing, hexane was evaporated off, resulting in Fe-oleate complex in a waxy form.

### Synthesis of magnetite nanocubes

Iron oleate (0.5 g), oleic acid (0.1 mL) and 1-octadecene (10 mL) were mixed in a three neck bottle flask and degassed under argon for 30 min at  $70 \text{ }^\circ\text{C}$ . The reaction mixture was heated to  $320 \text{ }^\circ\text{C}$  with a constant heating rate of  $5.5 \text{ }^\circ\text{C min}^{-1}$ , and then kept at that temperature for 30 minutes. When the reaction temperature reached  $320 \text{ }^\circ\text{C}$ , a severe reaction occurred and the initial transparent solution became turbid and brownish black. The resulting solution containing the nanocrystals was then cooled to room temperature, and the synthesized nanocrystals were precipitated using isopropanol and redispersed in hexane for further use.

### Silica coating on magnetite nanocubes

For the reverse microemulsion synthesis, IgePAL CO-520 (1.3 mL) was dispersed in cyclohexane (10 mL) and stirred for 15 min (500 rpm) to form a stable solution. Subsequently, a dispersion of nanocubes (0.5-1 nmol) in cyclohexane (1 mL) was added, followed by TEOS (80  $\mu\text{L}$ ) and ammonia (150  $\mu\text{L}$ ). Between the additions, the reaction mixture was stirred for 15 min (500 rpm). Once ammonia was added, the mixture was stirred for 2 days. Finally, the particles were purified by adding 25 mL of ethanol to the reaction mixture and centrifuging the whole mixture for 20 min at 9500 rpm. After removal of the supernatant, 25 mL of ethanol was added, and the silica particles were sedimented again by centrifugation at 9500 rpm for 20 min. This was repeated once more for 20 min, after which the particles were redispersed in 5 mL double distilled water and stored at  $4 \text{ }^\circ\text{C}$ .

### Characterization of the magnetite nanocubes

TEM, HR-TEM images and SAED pattern of nanocubes were obtained using a high resolution transmission electron microscope (TEM - Tecnai G2 F30) operating at 300 kV. UV-Vis absorption spectra were obtained using a UV-Vis spectrophotometer (Varian - Cary 100). FT-IR spectra was obtained by using an FT-IR spectrometer (Bruker-Vertex 70). Magnetic measurements (M-H and M-T curves) were recorded on Quantum Design MPMS-XL-7 system. MR phantom experiments were performed at room temperature on a 3T Siemens TrioTim MR scanner. Various concentrations (3 to 60  $\mu\text{M}$ ) of magnetite nanoparticles were prepared for MRI phantom study.  $T_1$ -weighted and  $T_2$ -weighted phantom MR images of magnetite nanoparticles were acquired using spin echo (SE) sequence under the following parameters: TR/TE = 1000/12 ms ( $T_1$ ), TR/TE = 10000/330 ms ( $T_2$ ), (slice thickness = 3 mm, flip angle =  $90^\circ$ , acquisition matrix = 384 pixels  $\times$  384 pixels, FoV =  $120 \times 120 \text{ mm}^2$ ).

### *in vivo* MR imaging

Animal experiments were performed using *Sprague Dawley* (200–250 g) rat according to a protocol approved by the animal ethics committee of Bilkent University, Turkey. MRI experiments were performed at room temperature on a 3T Siemens TrioTim MR scanner. Silica coated magnetite nanocubes with the dosage of 1 mg kg<sup>-1</sup> were injected into a rat through its tail vein and coronal images of the kidneys were taken before and after injection of magnetite nanocubes. T<sub>1</sub>-weighted and T<sub>2</sub>-weighted *in vivo* rat MR images were acquired using spin echo (SE) sequence under the following parameters: TR/TE = 550/11 ms (T<sub>1</sub>), TR/TE = 4420/94 ms (T<sub>2</sub>), (slice thickness = 2 mm, flip angle = 90°, acquisition matrix = 384 pixels × 384 pixels, FoV = 90 × 90 mm<sup>2</sup>).

### Cytotoxicity Studies

The *in vitro* cytotoxicity of iron oxides nanocubes was investigated using L929 mouse cell line. Silica coated iron oxides were added with the concentrations of 0, 25, 100 and 200 µg Fe/mL and toxic response was evaluated by Alamar Blue Assay after 24 hrs. To determine the viability, 2 × 10<sup>3</sup> L929 cells were seeded into 96 well plate (n=3) and silica coated cubic iron oxides were added in different concentrations in ddH<sub>2</sub>O. For the positive control, the cells were grown without exposure to the nanoparticle solution. In order to understand the fatal effect of less medium on the cells, we added phosphate buffer saline (PBS) with the same amount of ddH<sub>2</sub>O as negative control group for each concentration. Cells were cultured in Dulbecco's Modified Eagle Medium (DMEM) containing 10% fetal bovine serum (FBS) at 37 °C and 5% CO<sub>2</sub> for 24 h. Subsequently, the cells were incubated in Alamar Blue solution (10% in DMEM-high glucose colorless medium) at 37 °C for 1 h. After the desired incubation time, the supernatant (200 µL) was transferred into 96 well plate, and the absorbances at 570 and 595 nm were measured. A calibration curve was constructed using known concentrations of cells (L929) to relate the cell numbers to the dye reduction (%).

## Results and Discussion

Magnetite nanocubes were synthesized using thermal decomposition of iron-oleate complex using a modified recipe.<sup>28</sup> We observed that the shape and size of the iron oxide NPs can be controlled by varying the molar ratio of iron-oleate to oleic acid and by the heating rate. In Ref. 28, 12 nm sized spherical magnetite NPs were synthesized with the ratio of iron-oleate:oleic acid as 2:1 with a heating rate of 3.3 °C/min. In our case, cubic shaped magnetite NPs were obtained with increased oleic acid amount, i.e., equal molar ratio of iron-oleate and oleic acid, with a heating rate of 5.5 °C/min. The small but critical reduction in growth rate by the additional oleic acid appears to promote the formation of iron oxide NPs with nonspherical, faceted shape. **Fig. 1a** shows the magnetite nanocubes disperse in hexane and **Fig. 1b** shows TEM (transmission electron microscope) images of monodisperse magnetite nanocubes with an average size of 9.7 ± 0.5 nm. The particle size distribution (PSD) of the nanocubes obtained using ImageJ software is shown in **Fig. 1d**. XRD spectra of as synthesized iron oxide nanocubes are presented in supporting information (**Fig. S1**). From the XRD data, it is found that the reflections are closer to the magnetite structure of the iron oxide NPs (**Table S1** in supporting information). To further confirm

the structure these nanocubes, we have also performed, SAED, FT-IR and absorption spectra. Magnetite structure of the iron oxide nanocubes were confirmed by selected area electron diffraction (SAED) pattern<sup>29</sup>, Fourier transformed infrared spectra (FT-IR)<sup>28,30</sup> and optical absorption measurements.<sup>30</sup> We carried out SAED (**Fig. 1e**) of these nanocubes and found that the rings can be assigned to the spinel structure of magnetite (JCPDS#19-0629). The 220 ( $d = 2.9683$  Å) and 400 ( $d = 2.0956$  Å) phase in SAED pattern are exclusive to the structure of magnetite.<sup>29</sup> The highly crystalline nature of these nanocubes is demonstrated by the high-resolution (HR) TEM images as shown in **Fig. 1c**. HR-TEM also confirms that the spacing between the planes ( $d \sim 0.295$  nm) are close to the magnetite structure of iron oxide nanocubes.

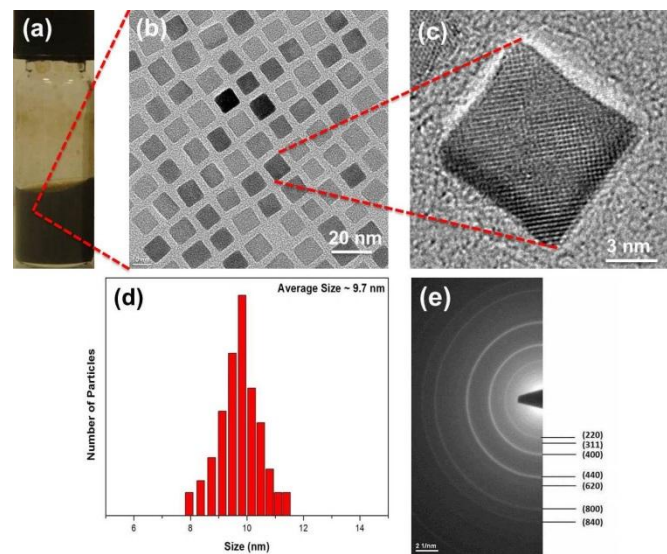


**Fig. 1** (a) Magnetite nanocubes dispersed in hexane. (b) TEM, (c) HR-TEM, (d) PSD and (e) SAED pattern of the as-synthesized magnetite nanocubes.

To further confirm the crystal structure of the as-synthesized iron oxide nanocubes, we performed absorption and FT-IR measurements. The nanocubes are easily dispersed in hexane to form transparent colloids, with a characteristic vivid color corresponding to the color of the bulk material. The absorption data are generally consistent with the characteristic color of the sample and are, therefore, considered as a reliable way of differentiating magnetite and maghemite structure of iron oxide. For Fe<sub>3</sub>O<sub>4</sub> nanocubes, the absorption spectrum exhibits a full absorption band in the visible area of 400–700 nm, which corresponds to the black color of the dispersion.<sup>30</sup> For α-Fe<sub>2</sub>O<sub>3</sub>, the strongest absorption peak appears at 400–450 nm and corresponds to the red color. In our case, the absorption spectrum exhibits a full absorption band in the visible area (**Fig. 2a**) along with the black color of the dispersion (**Fig. 1a**). Therefore, from the absorption data, it is clear that in our case the nanocubes possess magnetite structure.

FT-IR spectra of the iron-oleate complex and iron oxide nanocubes are presented in **Fig. 2b**. FT-IR was used to identify the functional groups present in the nanocubes. The wide band at 3130–3630 cm<sup>-1</sup> is assigned to O-H vibrations. The sharp bands at 2923 and 2853 cm<sup>-1</sup> are assigned to the asymmetric methyl stretching and

the asymmetric and symmetric methylene stretching modes, respectively. The sharpness of the bands is attributed to the well-ordered, long hydrocarbon chain of oleic acid. The characteristic bands at 1560 and 1443  $\text{cm}^{-1}$  can be attributed to the asymmetric and symmetric  $\text{COO}^-$  stretches, indicating that the oleic acid chain is attached in a bidentate fashion, with both oxygens symmetrically coordinated to the surface.<sup>31</sup> Based on the FT-IR spectra, oleic acid is thought to coat the surface of the nanocubes. TEM results, in conjunction with FT-IR data, suggest that, in our case we have a core-shell structure, with iron oxide core and oleate shell ( $\sim 1.6$  nm). This is also confirmed by uniform spacing between the nanocubes (see **Fig. 1b**). FT-IR is also used as a tool to distinguish magnetite and maghemite structures from each other through their distinct lattice absorption peaks.<sup>14</sup> The lattice absorption peaks of the iron oxide nanocubes centered at  $\sim 595$   $\text{cm}^{-1}$  (**Fig. 2b**) indicates that the nanocubes are most probably magnetite.<sup>32,33</sup> Therefore, on the basis of the SAED pattern, optical absorption data and FT-IR measurements, we confirm that these iron oxide nanocubes possess magnetite structure.

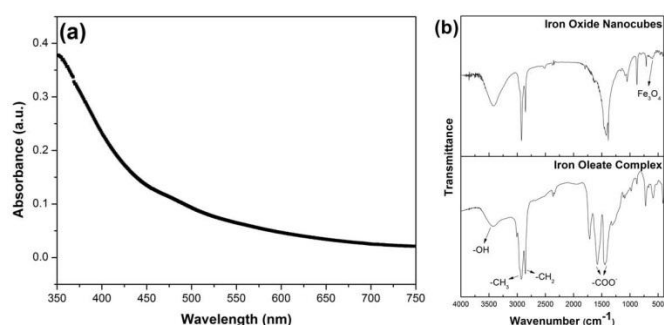


**Fig. 2** (a) Absorption spectra of the as-synthesized magnetite nanocubes. (b) FT-IR spectra of the as-synthesized magnetite nanocubes and iron-oleate complex.

We also studied the magnetic properties of these nanocubes using Quantum Design MPMS-XL-7 system. The magnetization dependence on magnetic field (M-H curve) of the magnetite nanocubes were measured at body temperature (310 K). We did the measurements at body temperature because we want to use these materials in humans as MRI contrast agents. M-H curves as shown in **Fig. 3a**, indicate that the saturated magnetization ( $M_s$ ) of the as-synthesized magnetite nanocubes ( $\sim 18$  emu/g) is much lower than that of magnetite NPs with a similar size ( $\sim 65$  emu/g) measured at room temperature.<sup>34</sup> Moreover, the continuous growth of magnetization along with the applied magnetic field for magnetite nanocubes is probably due to the enhanced spin canting effect in the surface layer of these nanocubes because of the size and shape,<sup>35</sup> which may be responsible for the partially paramagnetic property of these nanocubes. The characteristic M-H curves of these nanocubes are similar to those of the high-spin paramagnetic rare-earth materials and superparamagnetic nanoparticles,<sup>36</sup> suggesting that these nanocubes exhibit both superparamagnetic and paramagnetic behaviors. The presence of mixed magnetic phases is further confirmed by fitting the M-H curves with the following relation:

$$M(T) = M_s \left[ \coth \left( \frac{\mu H}{k_B T} \right) - \left( \frac{k_B T}{\mu H} \right) \right] + \chi H \quad (1)$$

where,  $M(T)$  is the magnetization of the nanocubes at temperature  $T$ ,  $M_s$  represents the saturation magnetization of the nanocubes,  $\mu$  is the magnetic moment of the nanocubes,  $\chi$  is the susceptibility of the nanocubes and  $k_B$  is the Boltzmann constant. The first term in Equation (1) is the superparamagnetic contribution and the second term is the paramagnetic contribution to the total magnetic moment of the nanocubes. The M-H fit obtained by using Equation (1) is shown in red color in **Fig. 3a**. Equation 1 is in excellent agreement with the experimental data, substantiating the simultaneous presence of two magnetic phases in the nanocubes. Therefore, we conclude that these nanocubes possess superparamagnetic and paramagnetic phases simultaneously, which result in simultaneous contrast enhancement in  $T_1$  and  $T_2$ -weighted MR images similar to GdIO NPs.<sup>10</sup>

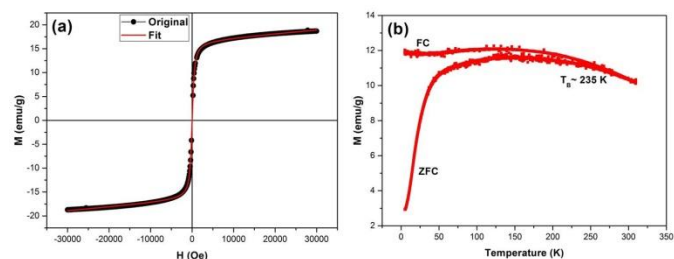


**Fig. 3** Magnetic properties; (a) M-H and (b) M-T curve of the as-synthesized magnetite nanocubes.

We also studied the magnetization ( $M$ ) dependence (zero field cooled - ZFC and field cooled - FC curves) on temperature ( $T$ ) of the as-synthesized magnetite nanocubes. The ZFC and FC curves, which coincide initially, start to separate and follow different trends as the temperature is decreased from 310 to 5 K. In the FC mode at the field level of  $H = 100$  Oe, the magnetization increases slightly and then levels off (**Fig. 3b**), whereas the ZFC magnetization reaches a maximum followed by a steady decrease to a value approaching zero in the low temperature region. The shape of the FC curves is the result of the presence of dipole-dipole interactions between the oleate-capped magnetite nanocubes.<sup>37</sup> Moreover, the variation of the magnetization in the ZFC and FC modes indicates a dominant superparamagnetic behavior for the magnetite nanocubes. The value of the blocking temperature for the nanocubes is estimated to be 235 K, obtained from Stoner-Wohlfarth relation:

$$T_B = \frac{K}{25k_B} * V \quad (2)$$

where  $T_B$  is the blocking temperature,  $K$  is the anisotropy constant,  $V$  is the volume of the nanocubes, and  $k_B$  is the Boltzmann constant. Similar values of the blocking temperature for iron oxide NPs are reported by Caruntu *et al.*<sup>34</sup>

Magnetite nanocubes were made water soluble for MRI applications by silica coating using a recipe reported elsewhere.<sup>38</sup> The encapsulated nanoparticles showed excellent colloidal stability in water. The hydrodynamic diameter of the silica coated nanocubes in deionized (DI) water, measured by dynamic light scattering (DLS), was 27.8 nm (**Fig. S2** of supporting information). DLS measurements reveal that the nanocubes are monodisperse with no aggregation. The hydrodynamic diameter value is less than 30 nm. Therefore, these nanocubes come in the category of ultra-small iron oxide nanocubes (USIONS). Hydrodynamic diameter is an important

parameter for the use of contrast agents in the human body. Our nanocubes hydrodynamic size lies between 43 nm<sup>22</sup> (maximum  $r_2$  relaxivity  $\sim 761 \text{ mM}^{-1}\text{s}^{-1}$  reported) and 15 nm<sup>23</sup> sized nanoparticles ( $r_1$  relaxivity  $\sim 4.78 \text{ mM}^{-1}\text{s}^{-1}$ ). Our coated nanocube size ( $\sim 27.8 \text{ nm}$ ) is close to the median to these two values. Therefore, we believe that because of the size and shape (enhanced spin-canting effect) of our nanocubes, they have the ability to enhance the contrast in both T<sub>1</sub>- and T<sub>2</sub>-weighted MRI.

The utility of the water-soluble magnetite nanocubes as DMCA for MR phantom studies was investigated in solution. Nanocubes were studied by a 3T Siemens MR scanner to observe the contrast enhancement in both T<sub>1</sub>- and T<sub>2</sub>-weighted MR images. **Fig. 4a** shows the T<sub>1</sub>-weighted MR images of silica capped magnetite nanocubes at different concentrations. We can clearly observe the increase in the image contrast (bright) with the increase in nanocubes concentration.

To examine the feasibility of using magnetite nanocubes as simultaneous T<sub>1</sub> and T<sub>2</sub> MRI contrast agent, the relaxation time was measured. The relaxation time T<sub>1,2</sub> was measured at 3T @ 25 °C using a Spin Echo sequence. The longitudinal ( $r_1$ ) and transverse ( $r_2$ ) relaxivity were determined from the following relation:

$$r_{1,2}[\text{Fe}_3\text{O}_4] = \frac{1}{T_{1,2}} - \frac{1}{T_0} \quad (3)$$

where,  $T_0$  and  $T_{1,2}$  are the longitudinal and transverse relaxation times of DI water and the samples with increasing nanocubes concentration, respectively.<sup>39</sup> From the slope of  $(1/T_1 - 1/T_0)$  versus nanocubes concentration (**Fig. 4b**), we obtain the longitudinal relaxivity ( $r_1$ ) as  $5.23 \text{ mM}^{-1}\text{s}^{-1}$ . The high  $r_1$  relaxivity of the magnetite nanocubes can be attributed to the large number of Fe<sup>3+</sup> ions with 5 unpaired electrons on the surface of the nanocubes. This value is higher than the value reported for 3 nm sized spherical iron oxide nanoparticles,<sup>23</sup> which most probably resulted from the shape of our nanocubes as suggested by Zhen *et al.*<sup>25</sup> Recently, Zhou *et al.*<sup>26</sup> reported T<sub>1</sub> contrast enhancement in Fe<sub>3</sub>O<sub>4</sub> nanoplates with (111) exposed surfaces. In our case too, there may be some contribution to the T<sub>1</sub> contrast from the exposed surfaces of the magnetite nanocubes.

**Fig. 4c** shows the T<sub>2</sub>-weighted MR images of silica capped magnetite nanocubes at different concentrations. Here, we can clearly observe the decrease in the image contrast (dark) with the increasing nanocubes concentration. The transversal relaxivity ( $r_2$ ) value of nanocubes obtained from the slope of  $(1/T_2 - 1/T_0)$  versus nanocubes concentration (**Fig. 4d**) is  $89.68 \text{ mM}^{-1}\text{s}^{-1}$ . Magnetite nanocubes exhibit low T<sub>2</sub> relaxivity as compared to the larger sized particles because the low magnetic moment induces weak magnetic inhomogeneity around the particles.<sup>22</sup>

Thus, with increased concentrations of magnetite nanocubes, we observed reduced signals in T<sub>2</sub>-weighted MR images and increased signal in T<sub>1</sub>-weighted MR images, indicating that magnetite nanocubes can act as both negative and positive contrast agents simultaneously. Iron oxide NPs are well known for their excellent T<sub>2</sub> contrast enhancement effect with no obvious T<sub>1</sub> contrast effect. By decreasing the size of magnetic NPs, they are also reported as potential T<sub>1</sub> contrast agents.<sup>23,40</sup>

By fine tuning the shape of the iron oxide nanoparticles into cubes and making their size ultra-small, here we aim at achieving simultaneous enhancement in both positive and negative

MR contrast images. In our case, we conclude that our nanocubes shape and dimension combinedly results in the simultaneous contrast enhancement in both T<sub>1</sub>- and T<sub>2</sub>-weighted MRI, which we do not observe otherwise individually.

The *in vitro* cytotoxicity of magnetite nanocubes was investigated using L929 mouse cell line with the concentrations of 0, 25, 100 and 200 µg Fe/mL in ddH<sub>2</sub>O. No appreciable toxicity was observed even at very high concentrations of 100 µg Fe/mL (**Fig. S3** in the supporting information), which is consistent with the recent report by Wortmann *et al.*<sup>41</sup> On the other hand, further addition of cubic iron oxide decreased the viability of L929 cell. The result of cell assays confirmed that the silica coated iron oxide nanocubes are not significantly cytotoxic, up to high concentrations of 100 µg Fe/ml.

We further study the *in vivo* MR imaging of the kidneys of rat using these nanocubes. For *in vivo* MR imaging, T<sub>1</sub> and T<sub>2</sub> dual-mode abdominal images before and after injection was obtained by using a 3T MR scanner at room temperature. Silica coated magnetite nanocubes with the dosage of 1 mg kg<sup>-1</sup> were injected into a rat through its tail vein and coronal images of the kidneys were taken before injection, immediately after injection, and after 30 and 60 min of injection (**Fig. 5**). Since the kidney is an important member of urinary system and one of its functions is a filtration of waste products from the body, we focused on the kidneys in the MR imaging. With the post injection time, the blood vessels going into kidneys gradually turned to brighter and darker in T<sub>1</sub> and T<sub>2</sub> coronal planes, respectively. Color images of the kidney is shown in the insets of **Fig. 5** for clarity. These results demonstrated that although our silica coated cubic nanoparticles have a hydrodynamic diameter (HD) of 27.8 nm, they can be observed in the kidneys where the renal cut-off is being 5–6 nm. This may be due to the coating material, “silica”. There are several reports<sup>42,43</sup> on the renal clearance of silica coated nanoparticles revealed intact and larger particles in the urine; however, the exact excretion process remained unclear. In order to understand the clearance mechanism involving silica, Lu *et al.*<sup>44</sup> investigated the biodistribution of silica nanoparticles with diameters of ca. 100–130 nm. They observed a rapid excretion of almost all of the nanoparticles from the body through urine and feces. Similar results were also observed by He *et al.*<sup>45</sup> revealing that the silica nanoparticles of ca. 45 nm accumulated mainly in the liver, kidney, and urinary bladder a few hours after intravenous injection and consequently silica nanoparticles are safely removed through the renal route. All of these previous works clearly show that very large nanoparticles can be efficiently removed from the body via renal excretion. In the light of these studies, we can attribute the excretion of our nanoparticles to the silica coating which may help particles to escape RES recognition by possibly limiting the opsonization of nanoparticles<sup>46</sup> and guiding them to the renal clearance. Furthermore, the intravenous injection might also take role in the rapid renal excretion of our nanoparticles as reported by He *et al.*<sup>45</sup> In addition, similar to Ref. 44, it is also possible that our nanoparticles degrade quickly in the bloodstream and the smaller particles may then prefer renal clearance. However, a more detailed analysis on the clearance mechanism of the silica coated iron oxide nanoparticles larger than 6 nm can be investigated as a subject of another study for a better and deeper understanding.

## ARTICLE

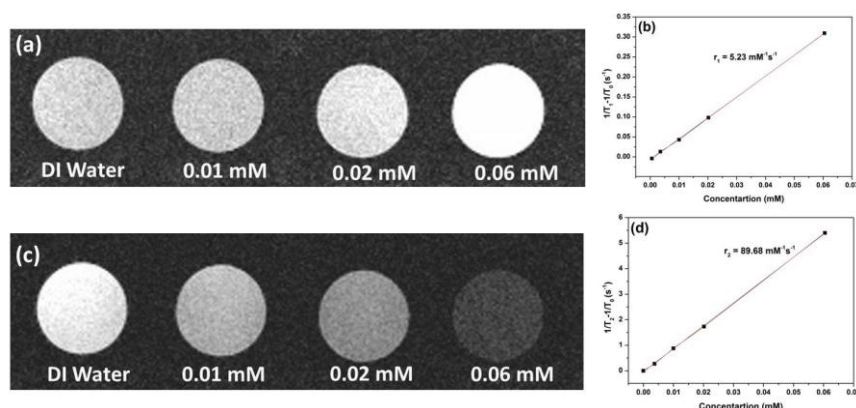


**Fig. 4** (a)  $T_1$ -weighted and (c)  $T_2$ -weighted MR phantom images of the as-synthesized magnetite nanocubes. (b)  $T_1$  and (d)  $T_2$  relaxivity plots of the as-synthesized magnetite nanocubes obtained at 3 Tesla @ 25 °C.

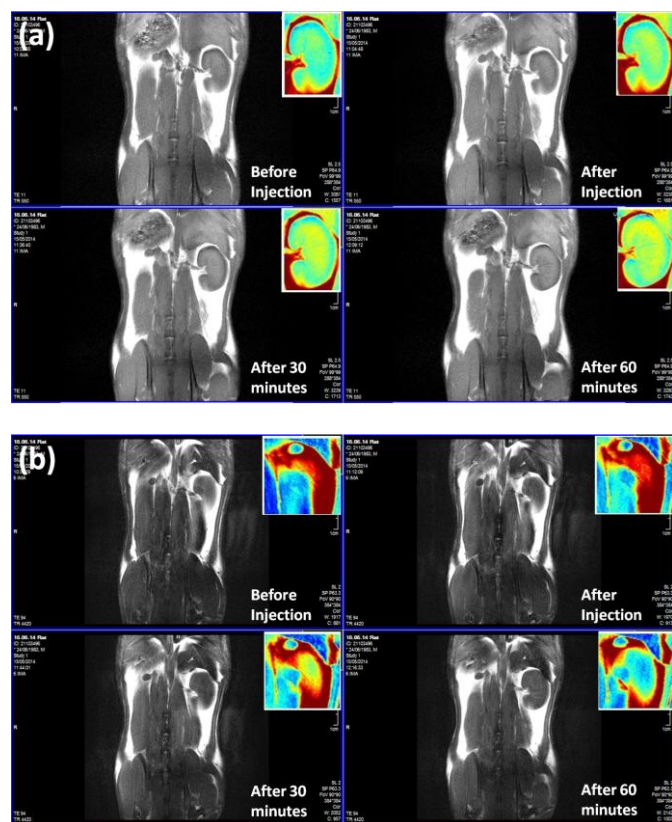


**Fig. 5** (a)  $T_1$ - and (b)  $T_2$ -weighted *in vivo* MR images obtained before and after the nanocubes injection into the rat, at 3 Tesla @ 25 °C. In the inset, the kidney images in color are shown for the clear enhancement in the contrast.

In summary, our experiments demonstrated that these nanocubes are suitable as a contrast agent for MRI owing to their strong MR contrast enhancement in both  $T_1$ - and  $T_2$ - weighted imaging. Because of their dual-mode contrast feature and high biocompatibility, they allow access to comprehensive information with higher accuracy in medical diagnosis.

## Conclusions

In this work, we have synthesized highly crystalline, monodisperse and low-magnetization magnetite nanocubes that achieve simultaneously enhance contrast in  $T_1$ - and  $T_2$ -weighted MR images. The dual-mode MR contrast enhancement capabilities of these nanocubes are a direct result of the simultaneous presence of superparamagnetic and paramagnetic phases as confirmed by the magnetic measurements. Also, these nanocubes are small in size (~9.7 nm) and almost harmless for use in the human body. These nanocubes while being non-toxic and bio-compatible, hold great promise as DMCAs for better diagnosis of patients using MRI.

## Acknowledgements

The authors would like to thank the EU-FP7 Nanophotonics4Energy NoE, TUBITAK EEEAG 109E002, 109E004, 110E010, 110E217, NRF-RF-2009-09, NRF-CRP-6-2010-02, and A\*STAR of Singapore for the financial support. H.V.D. acknowledges support from ESF-EURYI and TUBA-GEBIP. We would like to acknowledge Biomaten (METU), in particular Prof. Vasif Hasirci, Dr. Arda Buyuksungur and Tugba Dursun for cytotoxicity experiments. Also, we would like to acknowledge Dr. U. O. S. Seker (UNAM) for his valuable discussions.

## Notes and references

<sup>a</sup>UNAM-Institute of Materials Science and Nanotechnology, National Magnetic Resonance Research Center (UMRAM), Department of Electrical and Electronics Engineering, Department of Physics, Department of Molecular Biology and Genetics, Bilkent University, Ankara, 06800, Turkey

<sup>b</sup>LUMINOUS! Center of Excellence for Semiconductor Lighting and Displays, School of Electrical and Electronic Engineering, School of Mathematical and Physical Sciences, Nanyang Technological University, Singapore 639798, Singapore

E-mail: [volkan@bilkent.edu.tr](mailto:volkan@bilkent.edu.tr); [hvdemir@ntu.edu.sg](mailto:hvdemir@ntu.edu.sg)

- 1 N. Lee and T. Hyeon, *Chem. Soc. Rev.*, 2012, **41**, 2575–89.
- 2 M. Srinivas, E. H. J. G. Aarntzen, J. W. M. Bulte, W. J. Oyen, a Heerschap, I. J. M. de Vries and C. G. Figdor, *Adv. Drug Deliv. Rev.*, 2010, **62**, 1080–93.
- 3 Y. Piao, J. Kim, H. Bin Na, D. Kim, J. S. Baek, M. K. Ko, J. H. Lee, M. Shokouhimehr and T. Hyeon, *Nat. Mater.*, 2008, **7**, 242–7.
- 4 E. I. Galanzha, E. V Shashkov, T. Kelly, J.-W. Kim, L. Yang and V. P. Zharov, *Nat. Nanotechnol.*, 2009, **4**, 855–60.
- 5 H. Bin Na, I. C. Song and T. Hyeon, *Adv. Mater.*, 2009, **21**, 2133–2148.
- 6 Y.-X. J. Wang, *Quant. Imaging Med. Surg.*, 2011, **1**, 35–40.
- 7 D. Pan, A. H. Schmieder, S. a Wickline and G. M. Lanza, *Tetrahedron*, 2011, **67**, 8431–8444.
- 8 P. Caravan, J. J. Ellison, T. J. McMurry and R. B. Lauffer, *Chem. Rev.*, 1999, **99**, 2293–352.
- 9 D. Choi, A. Han, J. P. Park, J. K. Kim, J. H. Lee, T. H. Kim and S.-W. Kim, *Small*, 2009, **5**, 571–3.
- 10 Z. Zhou, D. Huang, J. Bao, Q. Chen, G. Liu, Z. Chen, X. Chen and J. Gao, *Adv. Mater.*, 2012, **24**, 6223–6228.
- 11 W. Chen, F. Lu, C.-C. V Chen, K.-C. Mo, Y. Hung, Z.-X. Guo, C.-H. Lin, M.-H. Lin, Y.-H. Lin, C. Chang and C.-Y. Mou, *NMR Biomed.*, 2013, **26**, 1176–85.
- 12 K. H. Bae, Y. B. Kim, Y. Lee, J. Hwang, H. Park and T. G. Park, *Bioconjug. Chem.*, 2010, **21**, 505–512.
- 13 S.-J. Cho, B. R. Jarrett, A. Y. Louie and S. M. Kauzlarich, *Nanotechnology*, 2006, **17**, 640–644.
- 14 F. Hu, Q. Jia, Y. Li and M. Gao, *Nanotechnology*, 2011, **22**, 245604.
- 15 G. Huang, H. Li, J. Chen, Z. Zhao, L. Yang, X. Chi, Z. Chen, X. Wang and J. Gao, *Nanoscale*, 2014, **6**, 10404–12.
- 16 J.-S. Choi, J.-H. Lee, T.-H. Shin, H.-T. Song, E. Y. Kim and J. Cheon, *J. Am. Chem. Soc.*, 2010, **132**, 11015–7.
- 17 M. Cho, R. Sethi, J. S. Ananta narayanan, S. S. Lee, D. N. Benoit, N. Taheri, P. Decuzzi and V. L. Colvin, *Nanoscale*, 2014, **6**, 13637–13645.
- 18 G. Huang, X. Zhu, H. Li, L. Wang, X. Chi, J. Chen, X. Wang, Z. Chen and J. Gao, *Nanoscale*, 2015, **7**, 2667–2675.
- 19 E. a Neuwelt, P. V árallyay, a G. Bag ó L. L. Muldoon, G. Nesbit and R. Nixon, *Neuropathol. Appl. Neurobiol.*, 2004, **30**, 456–71.
- 20 A. H. Kaim, T. Wischer, T. O'Reilly, G. Jundt, J. Fröhlich, G. K. von Schulthess and P. R. Allegrini, *Radiology*, 2002, **225**, 808–14.
- 21 K. H. Bae, M. Park, M. J. Do, N. Lee, J. H. Ryu, G. W. Kim, C. Kim, T. G. Park and T. Hyeon, *ACS Nano*, 2012, **6**, 5266–73.
- 22 N. Lee, Y. Choi, Y. Lee, M. Park, W. K. Moon, S. H. Choi and T. Hyeon, *Nano Lett.*, 2012, **12**, 3127–31.
- 23 B. H. Kim, N. Lee, H. Kim, K. An, Y. Il Park, Y. Choi, K. Shin, Y. Lee, S. G. Kwon, H. Bin Na, J.-G. Park, T.-Y. Ahn, Y.-W. Kim, W. K. Moon, S. H. Choi and T. Hyeon, *J. Am. Chem. Soc.*, 2011, **133**, 12624–31.
- 24 Z. Li, P. W. Yi, Q. Sun, H. Lei, H. Li Zhao, Z. H. Zhu, S. C. Smith, M. B. Lan and G. Q. (Max) Lu, *Adv. Funct. Mater.*, 2012, **22**, 2387–2393.
- 25 G. Zhen, B. W. Muir, B. a Moffat, P. Harbour, K. S. Murray, B. Mobaraki, K. Suzuki, I. Madsen, N. Agron-Olshina, L. Waddington, P. Mulvaney and P. G. Hartley, *J. Phys. Chem. C*, 2011, **115**, 327–334.
- 26 Z. Zhou, Z. Zhao, H. Zhang, Z. Wang, X. Chen, R. Wang, Z. Chen and J. Gao, *ACS Nano*, 2014, **8**, 7976–7985.
- 27 J. Huang, L. Bu, J. Xie, K. Chen, Z. Cheng, X. Li and X. Chen, *ACS Nano*, 2010, **4**, 7151–7160.
- 28 J. Park, K. An, Y. Hwang, J.-G. Park, H.-J. Noh, J.-Y. Kim, J.-H. Park, N.-M. Hwang and T. Hyeon, *Nat. Mater.*, 2004, **3**, 891–5.
- 29 a. Shavel, B. Rodríguez-González, M. Spasova, M. Farle and L. M. Liz-Marzán, *Adv. Funct. Mater.*, 2007, **17**, 3870–3876.
- 30 X. Liang, X. Wang, J. Zhuang, Y. Chen, D. Wang and Y. Li, *Adv. Funct. Mater.*, 2006, **16**, 1805–1813.



- 31 A. a Khaleel, *Chemistry*, 2004, **10**, 925–32.
- 32 Y.-W. Jun, Y.-M. Huh, J.-S. Choi, J.-H. Lee, H.-T. Song, S. Kim, S. Yoon, K.-S. Kim, J.-S. Shin, J.-S. Suh and J. Cheon, *J. Am. Chem. Soc.*, 2005, **127**, 5732–3.
- 33 F. Hu, Z. Li, C. Tu and M. Gao, *J. Colloid Interface Sci.*, 2007, **311**, 469–74.
- 34 D. Caruntu, G. Caruntu and C. J. O'Connor, *J. Phys. D. Appl. Phys.*, 2007, **40**, 5801–5809.
- 35 M. P. Morales, S. Veintemillas-Verdaguer, M. I. Montero, C. J. Serna, A. Roig, L. Casas, B. Martínez and F. Sandiumenge, *Chem. Mater.*, 1999, **11**, 3058–3064.
- 36 G. F. Goya, T. S. Berquó, F. C. Fonseca and M. P. Morales, *J. Appl. Phys.*, 2003, **94**, 3520.
- 37 L. Suber, P. Imperatori, G. Ausanio, F. Fabbri and H. Hofmeister, *J. Phys. Chem. B*, 2005, **109**, 7103–9.
- 38 E. M. Hutter, F. Pietra, R. J. A. van Dijk - Moes, D. Mitoraj, J. D. Meeldijk, C. de Mello Doneg áand D. Vanmaeckelbergh, *Chem. Mater.*, 2014, **26**, 1905–1911.
- 39 E. A. Weitz, C. Lewandowski, E. D. Smolensky, M. Marjańska and V. C. Pierre, *ACS Nano*, 2013, **7**, 5842–5849.
- 40 L. Zeng, W. Ren, J. Zheng, P. Cui and A. Wu, *Phys. Chem. Chem. Phys.*, 2012, **14**, 2631–6.
- 41 L. Wortmann, S. Ilyas, D. Niznansky, M. Valldor, K. Arroub, N. Berger, K. Rahme, J. Holmes and S. Mathur, *ACS Appl. Mater. Interfaces*, 2014, **6**, 16631–16642.
- 42 X. Huang, L. Li, T. Liu, N. Hao, H. Liu, D. Chen and F. Tang, *ACS Nano*, 2011, **5**, 5390–5399.
- 43 V. Mamaeva, C. Sahlgren and M. Lind é, *Adv. Drug Deliv. Rev.*, 2013, **65**, 689–702.
- 44 J. Lu, M. Liong, Z. Li, J. I. Zink and F. Tamanoi, *Small*, 2010, **6**, 1794–1805.
- 45 X. He, H. Nie, K. Wang, W. Tan, X. Wu and P. Zhang, *Anal. Chem.*, 2008, **80**, 9597–9603.
- 46 M. Longmire, P. L. Choyke and H. Kobayashi, *Nanomedicine*, 2008, **3**, 703–717.